Numerical investigation of two-phase flows in highly-permeable porous media: Effect of the permeability on the drag force between fluid phases

Maxime Cochennec, Hossein Davarzani, Yohan Davit
Ioannis Ignatiadis, Michel Quintard

May 3, 2020

The macroscopic description of two-phase flows in porous media requires accurate modelling of the drag forces between the two fluids and the solid phase. In standard porous media, where capillarity is often dominant, the fluids-solid interactions are well-known and the fluid-fluid drag force is neglected in the momentum transport equation. Two-phases flows in high permeability porous media, however, are often characterized by a larger area of the interface between the two fluids and the development of thin films. In such cases, the fluid-fluid interaction is not necessarily negligible and may play an important role in the momentum transport equations. Here, we use computational methods to study two-phase flows in a microfluidic device made of an array of cylinders sandwiched in a Hele-Shaw cell. The idea is to keep the geometry in the cell plane unaltered, while changing the height in the orthogonal direction, i.e. the cell plates aperture h, to explore different ranges of permeability. This was done by taking advantage of the quasi-planar nature of the flow which justifies the use of depth-averaged flow equations. Here we reproduce a film-flow regime and show that the drag exerted at the fluid-fluid interface is between 5% and 60% of the drag exerted upon the solid. Furthermore, we found that the drag exerted upon the fluid-fluid interface increases as h^{-3} while the solid-fluid drag increases as h^{-2}. Our results demonstrate that the fluid-fluid drag force should not be neglected in momentum tranport equations when modelling macroscopic two-phase flows in microfluidic devices or highly permeable porous media, for which the film-flow regime is commonly encountered.

1. Introduction

An accurate description of two-phase flows in high-permeability porous media is of major importance in several practical applications. This includes soil remediation in gravely soils (Fetter et al., 2017), nuclear safety (Clavier et al., 2017) or catalytic fixed bed reactors (de Santos et al., 1991). However, most of the literature on the topic is focused on two-phase flow in low-permeability porous media.

For low-permeability porous media, the flow is often dominated by surface tension forces, and the capillary, Bond, and Weber numbers are low. In this case, the fluid repartition is well described as two independent flow channels (Blunt, 2017; Dullien, 2012). The two fluids are segregated, the non-wetting fluid flowing into the larger pores while the wetting fluid occupies the smaller pores, and the area of the fluid-fluid interface is small, as illustrated in Fig. 1 (a).

In contrast, for high-permeability porous media, the flow is the result of a complex interaction between capillary, gravity, viscous, and inertial forces (Davit and Quintard, 2018). Capillary effects no longer dominate and the Weber, capillary, and Bond numbers may be

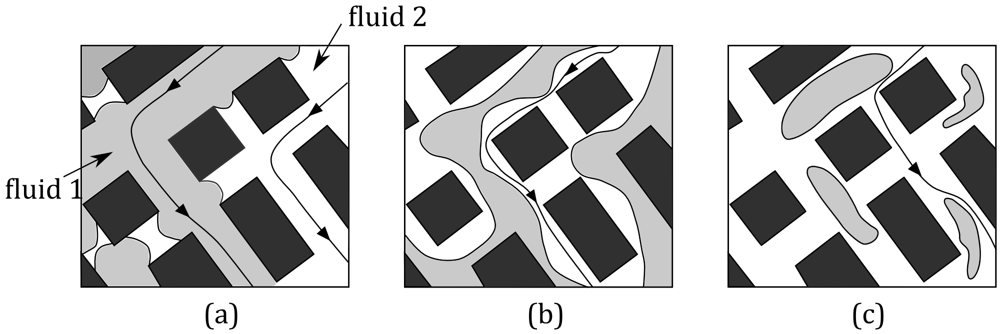

Figure 1: Illustration of possible fluids distributions in a 2D porous network with solid phase in black, the non-wetting fluid (fluid 1) in light grey, and the wetting fluid (fluid 2) in white, (a) the two fluids are flowing in different channels separated by numerous meniscus, (b) the wetting and non-wetting fluids are flowing together in most of the pores as two continuous streams and (c) both fluids are flowing together in most of the pores and the non-wetting phase is discontinuous. - Adapted from (Dullien, 2012)

large. Schematically, the fluids distribution in the pore space take two forms, either the non-wetting fluid is continuous and flowing in the center of the pore surrounded by the wetting fluid flowing as a thin film in contact with the solid, see Fig. 1 (b), or is discontinuous and flowing in the center of the pore as droplets or ganglias as in Fig. 1 (c). Here the surface area between the fluids is large and one would consider that the interaction forces between the fluids are not negligible compared to their counterpart between the fluid phases and the solid phase, in contrast with surface-tension dominated flow for which the area of the fluid-fluid interface is small. This is important because, as discussed in the following, these terms of surface forces between phases are the basis of any attempt to establish continuous relationships on a macroscopic scale starting from the pore scale and that the interaction between the fluids is commonly overlooked in the traditional model in porous media.

Indeed the ubiquitous continuous model used to describe two-phase flows in porous media is based on a direct extension of Darcy's equation and does not take into account the interaction between the fluids. The whole model, also known as Muskat equations (Wyckoff and Botset, 1936; Muskat, 1938), reads

$$0 = \frac{\partial \varepsilon S_i}{\partial t} + \nabla \cdot \mathbf{U}_i, \quad i = o, w, \tag{1a}$$

$$\mathbf{U}_i = -\frac{1}{\mu_i}\mathbf{K}_i \cdot (\nabla P_i - \rho_i \mathbf{g}), \quad i = o, w, \tag{1b}$$

$$1 = S_w + S_o, \tag{1c}$$

$$\mathbf{K}_w = \mathbf{K}\mathbf{k}_{rw}(S_w), \qquad \mathbf{K}_o = \mathbf{K}\mathbf{k}_{ro}(S_w), \tag{1d}$$

$$P_c(S_w) = P_o - P_w. \tag{1e}$$

where ε is the porosity, S_i is the saturation of fluid i, $\mathbf{U}_i$ is the intrinsic average velocity of fluid i, $\mathbf{K}$ is the absolute permeability tensor and P_i is the intrinsic average pressure of fluid i. The generalization toward two-phase flows involves the introduction of the relative permeability terms $\mathbf{k}_{ri}$ which account for the division of the void space between the fluids (Dullien, 2012), thus the relative permeability depends (non-linearly) only on the saturation. A constitutive relation between the macroscopic pressure of each fluid has to be furnished to close the set of the macroscopic equations. This relation is known as the capillary pressure relation and, as for the relative permeabilities, is supposed to depend non-linearly only on the saturation (Leverett et al., 1941).

Since the early 1980s, numerous work attempted to improve the generalized Darcy equations on a sound physical basis. Among them, several authors used upscaling techniques and found additional coupled permeability terms (Marle, 1982; Auriault and Sanchez-Palencia, 1986; Whitaker, 1986; Lasseux et al., 1996). The average momentum transport equations read

$$\mathbf{U}_i = -\frac{1}{\mu_i}\mathbf{K}^*_{ii} \cdot (\nabla P_i - \rho_i \mathbf{g}) - \frac{1}{\mu_j}\mathbf{K}^*_{ij} \cdot (\nabla P_j - \rho_j \mathbf{g}), \quad i, j = o, w \text{ and } i \neq j, \tag{2}$$

in which $\mathbf{K}^*_{ij}$ are the coupled relative permeability tensors that pertain to the interaction between the fluids. Several experimental works determined the coupled permeability from Equations (2) for a steady-state cocurrent flow of oil and water in sandpack. Each fluid was submitted alternatively to a null pressure gradient to isolate each term. This protocol was used by Zarcone and Lenormand (1994) and the authors found a negligible effect of the coupled permeabilities in the overall flow. With the same protocol with oil and water in a 2D-sandpack, Dullien and Dong (1996) found that the coupled permeabilities are important since they can contribute up to 35% of the effective permeability. Bentsen and Manai (1993) made cocurrent and countercurrent experiment to isolate each term, as proposed by Rose (1988), with water and oil in a sandpack found that coupled permeabilities reach, at least, 15% of the effective permeability value. However, it was pointed out that the saturation between the two sets of experiments can be very different and therefore the computed relative permeabilities can not be safely compared (Langaas and Papatzacos, 2001). The effect of the non-wetting phase connectivity on the transport parameters was extensively studied by Avraam and Payatakes (1995b), in which the authors performed steady-state cocurrent two-phase flow in 2D-micromodel experiments and found that the contribution of the coupled permeabilities on the flow is non-negligible and depend on the flow regimes. Recently, a whole analytical model for all the transport coefficients in Equation (2) has been derived for one-dimensional inertial two-phase flow in coarse non-consolidated porous media and which correctly predicts the pressure loss in debris beds (Clavier et al., 2017). Another approach, widely used in the literature on two-phase flow in packed-beds (de Santos et al., 1991; Carbonell, 2000), is to work with non-closed average momentum transport equations and to provide constitutive relations for the modeling of the interaction terms between the phases. These relations are obtained through the interpretation of experimental data (Sáez and Carbonell, 1985) or through theoretical developments (Tung and Dhir, 1988; Attou et al., 1999; Boyer et al., 2007).

In terms of numerical studies, the early work of Rothman (1990) examined the question of the interaction terms between the fluids by conducting two-phase flow simulations in simple geometries with an immiscible lattice-gas method. The author found non-negligible participation of the coupled permeabilities by applying the volume force alternatively on each fluid to isolate each term in Equations (2). Li et al. (2005) used the lattice-Boltzmann method and examined the value of the coupled permeabilities as a function of the saturation in a 3D-sphere pack and they found results in agreement with Rothman's results. Yiotis et al. (2007) also used a lattice-Boltzmann method in 2D and 3D pore networks and found a non-wetting apparent relative permeability greater than unity when the wetting fluid is more viscous than the non-wetting fluid. Recently Shams et al. (2018) have used a Volume Of Fluid method to study the transport coefficients of fluid layers in non-circular capillary tubes. Based on analogy with a model Couette flow the authors have derived simple relations that can predict with good accuracy the transport coefficients, including the coupled ones, of fluid layers.

The literature indicates that fluid interaction terms are mostly not negligible, but it is not yet clear what parameters control the value of these terms. In Figure 2 we present a comparison between some of the results available in the literature on coupled relative permeability values, adimensionalized with respect to the absolute permeability, and the analytical value obtained from steady-state two-phase flow in a capillary tube of circular cross-section (Bacri et al., 1990). This theoretical case represents a limit case regarding the large structure's permeability and the large extent of the fluid-fluid interface. The discrepancy between the results available in the literature and the value for this limit case could be explained by a smaller permeability if one based on the qualitative arguments given in this section about the relation between the permeability, the flow regime, and the extent of the fluid/fluid interface. What is important here is that the effect of the permeability is broader than the flow regime changes. Indeed the part of the interaction terms in the total pressure drop could decreases due to a reconfiguration of the fluids in the medium or because of the increasing friction exerted upon the solid structure by the fluids due to the lower permeability, while the value of the interaction terms between fluids would remain stable.

To form a better view of the relative interplay between the permeability, the friction exerted upon the solid, and the value of the interaction terms between the fluids, we performed direct numerical simulations in a micromodel. Micromodels are widely used for the great control of the flow regimes they offer. The different two-phase flow regimes have been investigated in such devices in several work (Avraam and Payatakes, 1995a; Salim et al., 2008; Horgue et al., 2013) and experiments have been recently conducted in quasi planar micromodels to investigate the interfacial interactions between two immiscible fluids (Heshmati and Piri, 2018; Roman et al., 2019). This paper follows this logic and clarifies the influence of the absolute permeability of the model porous medium on the interaction between fluids using numerical simulations. The original idea of the article lies in the use of depth-averaged equations to vary the permeability without having to change the geometry. It is organized as follows. In the next section averaged equations suitable for the study of two-phases quasi-planar flows are presented. In the section after the numerical method is presented, which is based on the level-set method for the tracking of the interface between fluids. Finally, the result section presents a study of the different interaction terms between the phases as a function of the capillary number of the flow and the absolute permeability of the model porous medium.

2. Theoretical background

In this section we derive the averaged flow equations for two-phases flows in a Hele-Shaw cell, starting from the three-dimensional Stokes equations. The system under consideration is depicted in Fig. 3 which represents a quasi-planar cocurrent two-phase flow between two parallel plates. The transverse dimension of the cell is noted L and h is the length of the

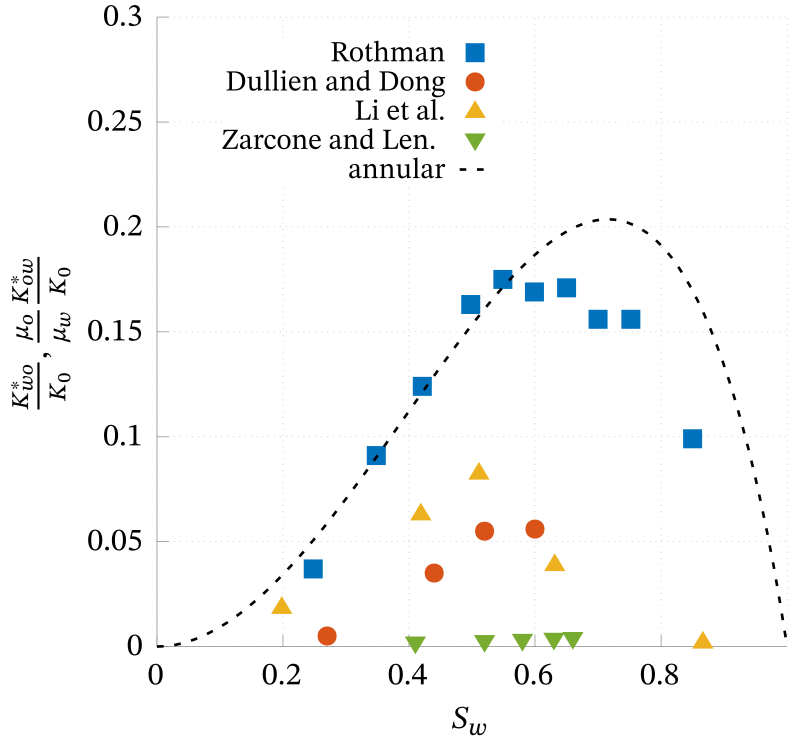

Figure 2: Adimensionalized coupled relative permeabilities from experimental work (Dullien and Dong, 1996; Zarcone and Lenormand, 1994) and numerical simulations (Rothman, 1990; Li et al., 2005) compared with and analytical solution for a steady-state annular two-phase flow in a circular capillary tube (dashed line) (Bacri et al., 1990).

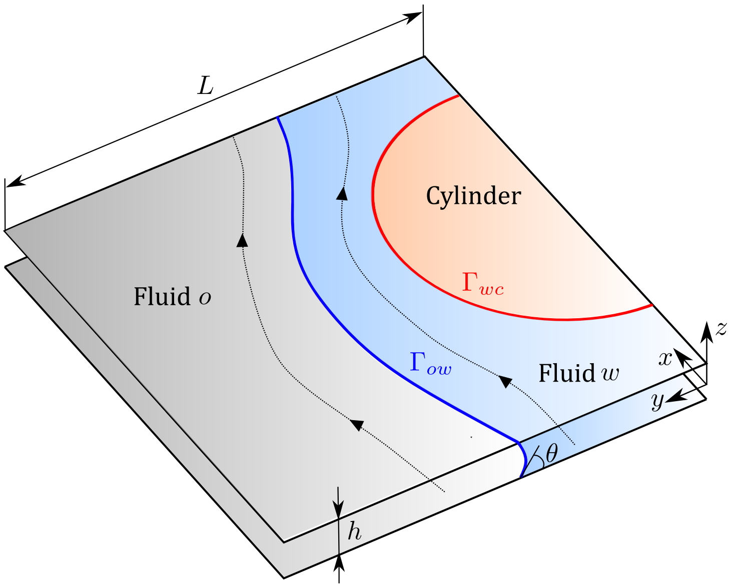

Figure 3: Schematic view of a cocurrent two-phase flow in a Hele-Shaw cell parallel to the $x-y$ plane with a wedge of circular cross-section as a solid obstacle. The transverse dimension of the cell is noted L while h denoted the aperture between the plates. The boundary Γ_{wc} between the fluid w and the cylinder is marked in red and the interface Γ_{ow} between the two fluids is marked in blue. The contact angle between the two fluids and the plates is noted θ.

aperture between the plates.

Depth averaging Three-dimensional continuity and Stokes equations for a Newtonian fluid in the absence of external forcing read, respectively,

$$\nabla \cdot \mathbf{u} = 0, \qquad -\nabla p + \mu \nabla^2 \mathbf{u} = 0. \tag{3}$$

Since the length scales in the z-direction are smaller than the length scales in the x, y directions, an order of magnitude estimation allows to rewrite Equations (3), at leading order, as

$$\nabla_{\parallel} \cdot \mathbf{u}_{\parallel} = 0, \qquad \mu \frac{\partial^2 \mathbf{u}_{\parallel}}{\partial z^2} = \nabla_{\parallel} p(x, y), \tag{4}$$

where the subscript $\mathbf{a}_{\|}$stands for the components in the x and y directions of vector $\mathbf{a}$. One can write

$$\mathbf{u}_{\|}(x,y,z) = (\bar{u}(x,y)f(z), \bar{v}(x,y)f(z), 0)^T, \tag{5}$$

again since the velocity variations in the x, y directions are much slower than the velocity variations in the z-direction. The depth-averaged velocity $\bar{\mathbf{u}} = \frac{1}{h}\int_{-h/2}^{h/2} \mathbf{u}_{\|}\, \mathrm{d}z$ is introduced and using its definition along with the no-slip boundary conditions at $z \pm h/2$, we obtain,

$$\mathbf{u}_{\|}(x,y,z) = \bar{\mathbf{u}}(x,y)\frac{3}{2}\left(1 - 4\frac{z^2}{h^2}\right). \tag{6}$$

Then, calculating the second derivative lead to,

$$\mu k^2 \bar{\mathbf{u}}(x,y) = -\nabla_{\|} p(x,y), \tag{7}$$

where $k^2 = 12/h^2$ is a permeability term. Equation (7) is valid in the limit of very small aspect ratio h/L and is analogous to the well known Darcy equation. To obtain a more versatile flow equation valid for moderate aspect ratio we recognise that the velocity profile is described by a parabolic profile in the z-direction but we reintroduce the second derivatives along the x, y directions. Then, equations (3) read,

$$\nabla_{\|} \cdot \bar{\mathbf{u}} = 0, \qquad \mu\left(\nabla_{\|}^2 \bar{\mathbf{u}} - k^2 \bar{\mathbf{u}}\right) = \nabla_{\|} p(x,y). \tag{8}$$

Equations (8) are the continuity and momentum transport equations for the depth-averaged flow of one fluid. Reproducing the velocity profile obtained from the three-dimensional Stokes equations for a flow in a channel with Equation (8) lead to a reasonable approximation up to aspect ratios of the order of $h/L = 1$ (Nagel and Gallaire, 2015). The approximation made by using on the reproduction of the velocity profile in a channel compared to the 3d results remains reasonable up to aspect ratios of 1. can In the case of two-phases flow, these equations have to be written for each fluid and boundary conditions at the fluid-fluid interfaces has to be given (Saffman and Taylor, 1958). Continuity of the depth-averaged velocities across the interface and a jump of interface normal stress are adequates if the surface tension is constant along the interface, and can be expressed as

$$\bar{\mathbf{u}}_o - \bar{\mathbf{u}}_w = 0 \text{ at } \Gamma_{ow}, \tag{9}$$

$$\left(\bar{\sigma}_{\|w} - \bar{\sigma}_{\|o}\right) \cdot \mathbf{n}_{\|ow} = \gamma \left(\frac{\pi}{4}\kappa_{\|} + \frac{2}{h}\cos\theta\right) \mathbf{n}_{\|ow} \text{ at } \Gamma_{ow}, \tag{10}$$

where $\bar{\sigma}_{\|i}$ is the in-plane stress tensor of fluid i, $\mathbf{n}_{\|ow}$ is the in-plane normal vector at the fluid interface pointing toward the fluid w, γ is the surface tension, $\kappa_{\|}$ is the in-plane interface curvature and θ denotes the contact angle between the fluid interface and the plates (see figure 3). The meniscus in the z direction is approximated as a half-circle of radius $h/2$ and the $\pi/4$ correction for the in-plane curvature was derived by Park and Homsy (1984). In Equation (10) we neglect aditionnal terms that pertain for the formation of dynamic film (Park and Homsy, 1984) which scaled non-linearly with the capillary number. We rather consider a non-zero contact angle an consequently the absence of such thin films.

Surface averaging Here we proceed to the spatial averaging of the in-plane momentum transport equations. We stop using the subscript $\|$ in the following since we work only with depth-averaged or two-dimensionnal quantities. We place ourselves in the volume averaging framework (Whitaker, 2013). Acknowledging that Equations (8) are two-dimensional, the traditional averaging theorem for some depth-averaged quantity $\bar{\omega}_i$ associated to the fluid i reads

$$\langle \nabla \bar{\omega}_i \rangle = \nabla \langle \bar{\omega}_i \rangle + \frac{1}{S} \int_{\Gamma_{ic}} \mathbf{n}_{ic} \bar{\omega}_i \, \mathrm{d}\Gamma + \frac{1}{S} \int_{\Gamma_{ij}} \mathbf{n}_{ij} \bar{\omega}_i \, \mathrm{d}\Gamma, \tag{11}$$

where,

$$\langle \bar{\omega}_i \rangle = \frac{1}{S} \int_{S_i} \bar{\omega}_i \, \mathrm{d}S, \tag{12}$$

is the superficial surface average and S is the surface of a representative elementary cell. Applying the superficial surface average of Equations (8) along with the averaging theorem and using traditional length-scale arguments we obtain

$$\frac{1}{S} \int_{\Gamma_{ic}} \mathbf{n}_{ic} \cdot \left(-p_i \mathbf{I} + \mu_i \left(\nabla \bar{\mathbf{u}}_i + (\nabla \bar{\mathbf{u}}_i)^T \right) \right) \mathrm{d}\Gamma + \frac{1}{S} \int_{\Gamma_{ij}} \mathbf{n}_{ij} \cdot \left(-p_i \mathbf{I} + \mu_i \left(\nabla \bar{\mathbf{u}}_i + (\nabla \bar{\mathbf{u}}_i)^T \right) \right) \mathrm{d}\Gamma - \\ - \mu_i k^2 \langle \bar{\mathbf{u}}_i \rangle = \varepsilon_i \nabla \langle p_i \rangle^i + \langle p_i \rangle^i \nabla \varepsilon_i, \quad i, j = o, w, \; i \neq j, \tag{13}$$

where $\mathbf{I}$ is the 2×2 identity matrix and $\langle p_i \rangle^i$ $\left(\langle p_i \rangle^i = \langle p_i \rangle / \varepsilon_i \right)$ is the intrinsic surface average pressure of fluid i, with ε_i the volume fraction of fluid i. The first integral is the drag force exerted upon the cylinders boundary by fluid i and the second integral pertains for the drag force exerted upon fluid j by fluid i. Two remarks must be made at this stage, firstly the presence of in-plane obstacle walls, depicted in Figure 3 by a wedge of circular cross-section, implies that the velocity field is three-dimensional near the obstacle because the flow is influenced by the no-flow condition over a distance of the order of the aperture h (Guyon et al., 1991) This also applies to the interface between fluids. A second point is that the integral on the fluid-fluid boundary interface is not strictly equivalent to an integral on this surface, here we make an approximation by considering that the contour in the $x - y$ plane can be identically translated along the z-direction, which is an approximation since the meniscus is a half-circle for small h/l. However, as shown in the appendix A, using three-dimensional flow simulations in microchannels, these approximations remain reasonable.

A more compact form of the Equations (13) can be written as

$$0 = -\varepsilon_w \nabla \langle p_w \rangle^w - \mu_w k^2 \langle \bar{\mathbf{u}}_w \rangle + \mathbf{d}_{wc} + \mathbf{d}_{wo}, \tag{14a}$$

$$0 = -\varepsilon_o \nabla \langle p_o \rangle^o - \mu_o k^2 \langle \bar{\mathbf{u}}_o \rangle + \mathbf{d}_{ow}, \tag{14b}$$

if the variation in space of the saturation is negligible and acknowledging that, as illustrated in Figure 3, only the wetting fluid w is in contact with the wedge. Here, $\mathbf{d}_{ij}$ denotes the drag forces per unit surface area exerted upon phase j by phase i and which must be computed or modeled to obtain closed macroscopic equations.

3. Direct numerical simulations

In this section we introduce the standard Level Set method to capture the moving free interface between the fluids along with the flow equations solved with the Finite Element solver Comsol Multiphysics.

3.1. Equations

Level Set model The Level Set method is part of Eulerian methods which have the particularity of easily reproducing topological changes of the phases contrary to Lagrangian methods. As topological changes of the fluids is not excluded here, this motivated our choice for this method.

In the Level Set framework, the fluid phases are identified with a level set (scalar) function that goes smoothly from 0 to 1 across the fluid interface, which is implicitly defined as the iso-level $\phi = 0.5$. Transport of the level set function ϕ is governed by

$$\frac{\partial \phi}{\partial t} + \nabla \cdot (\bar{\mathbf{u}} \phi) = \tau \nabla \cdot \left(\psi \nabla \phi - \phi (1 - \phi) \frac{\nabla \phi}{|\nabla \phi|} \right), \tag{15}$$

where $\bar{\mathbf{u}}$ is the depth-averaged velocity field and τ and ψ are two numerical parameters that control the diffuse interface thickness and the amount of re-initialization of ϕ function, respectively (Olsson et al., 2007). Remember that the differential operators have components only in the x, y directions.

Flow equations The flow equations to solve are analogous to the depth-averaged Equations (8) except that one continuity and momentum transport equation is valid for the whole domain and thus contribution of capillary forces is included in the momentum transport equation, as

$$0 = \nabla' \cdot \bar{\mathbf{u}} \tag{16a}$$

$$0 = -\nabla p + \mu(\phi)\left(\nabla^2 \bar{\mathbf{u}} - \frac{12}{h^2}\bar{\mathbf{u}}\right) + \gamma\left(\frac{\pi}{4}\nabla \cdot \left(\frac{\nabla\phi}{|\nabla\phi|}\right) - \frac{2}{h}\right)\delta(\phi)\mathbf{n}, \tag{16b}$$

where δ is the Dirac delta function localized on the interface and $\mathbf{n}$ denotes the unit normal to the interface, respectively defined as,

$$\delta(\phi) = 6\,|\nabla\phi|\,|\phi\,(1+\phi)|\,, \quad \text{and} \quad \mathbf{n} = \frac{\nabla\phi}{|\nabla\phi|}. \tag{17}$$

We introduce the following reference and dimensionless quantities,

$$\bar{\mathbf{u}} = \bar{\mathbf{u}}' \times U_r,\ p = p' \times \frac{\mu_r U_r}{L},\ \mathbf{x} = \mathbf{x}' \times L, \tag{18}$$

and thus the dimensionless continuity and momentum transport equations read,

$$0 = \nabla' \cdot \bar{\mathbf{u}}' \tag{19a}$$

$$0 = -\nabla' p' + \frac{\mu(\phi)}{\mu_r}\left(\nabla'^2 \bar{\mathbf{u}}' - \frac{12}{(h/L)^2}\bar{\mathbf{u}}'\right) + \frac{\gamma}{\mu_r U_r}\left(\frac{\pi}{4}\nabla' \cdot \left(\frac{\nabla'\phi}{|\nabla'\phi|}\right) - \frac{2}{h/L}\right)\delta'(\phi)\mathbf{n}, \tag{19b}$$

with $\delta'(\phi) = 6\,|\nabla'\phi|\,|\phi\,(1+\phi)|$. From Equation (19b) we note three dimensionless numbers, namely the viscosity ratio $M(\phi) = \frac{\mu(\phi)}{\mu_r}$, the capillary number $Ca^{-1} = \frac{\gamma}{\mu_r U_r}$ and the aspect ratio $h^* = h/L$. For a small apect ratio we can clearly see that the Darcean terms

Table 1: Boundary conditions for flow variables and the Level Set function.

Boundary	$\mathbf{u}$	p	ϕ
Outlet	-	0	$\mathbf{n} \cdot \nabla\phi = 0$
Inlet o	$1 - f_f$	-	0
Inlet w	f_f	-	1

become preponderant.

Geometry, boundary conditions and simulation parameters Our macroscopic model resembling a Hele-Shaw cell with wedges of cylindrical cross-section sandwiched between the plates as obstacles. This system is subdivided into five subdomains (Unit-Cell (UC)) encompassing one wedge, as depicted in Figure 4. Taking advantage of the symmetry, we studied only the upper half of a row. Each fluid flows from left to right (x direction) and boundary conditions used are summarized in Table 1. The reference velocity is the total inlet velocity, thus the dimensionless inlet velocities can be expressed as a fractional flow f_f,

$$f_f = \frac{u_w^x}{U_t}, \quad \text{with} \quad U_t = u_w^x + u_o^x. \tag{20}$$

The non-wetting viscosity is taken as the reference viscosity and the respective value of each dimensionless parameters are inventoried in Table 2. The viscosity ratio was chosen in favor of the invading fluid to mimic the invasion of an initially fully water-saturated micromodel by an oil-like fluid. The range of dimensionless aperture tested is large and the reader is warned that the depth-averaged equations derived in the previous section are outside their condition of validity for the extreme value $h/L = 5$, on the other hand, it provides a limit 2-dimensionnal case for information purposes.

Mesh convergence study Here we study the convergence of the various drag quantities we are interested in as a function of the number of mesh elements in the whole geome-

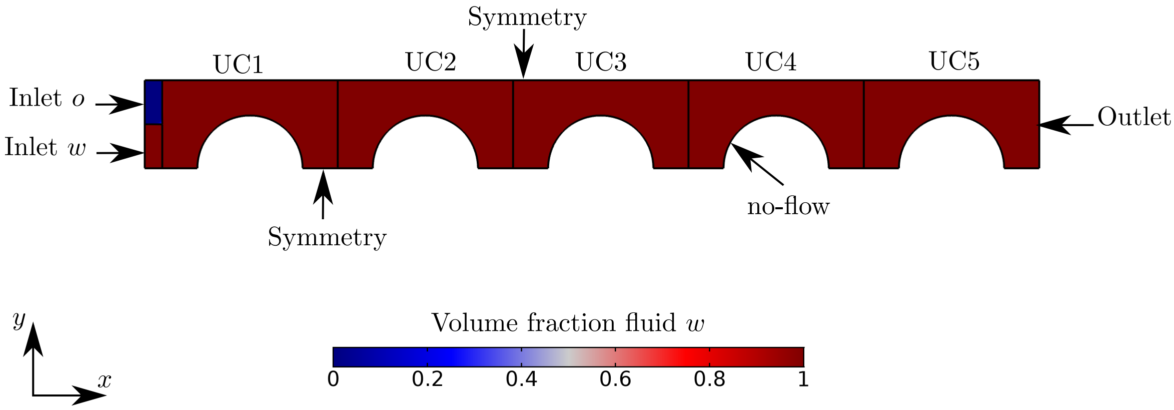

Figure 4: The geometry used is the superior half of an array of five cylindrical wedges inside five cuboid where both fluids are injected from left to right, initially the model is saturated with wetting fluid (in red), and the length of one Unit Cell (UC) is one millimetre. Symmetric boundary conditions are used on each length side and the no-flow boundary condition is enforced at the the wedge boundary.

Table 2: Simulation parameters and their respective values in the following work.

Parameters	Value
$Ca = \frac{U_t \mu_o}{\gamma}$	from 7.5×10^{-3} to 1
$M_w = \frac{\mu_w}{\mu_o}$	0.5
$f_f = \frac{u_w^x}{U_t}$	0.25
$h^* = h/L$	from 5 to 1/20

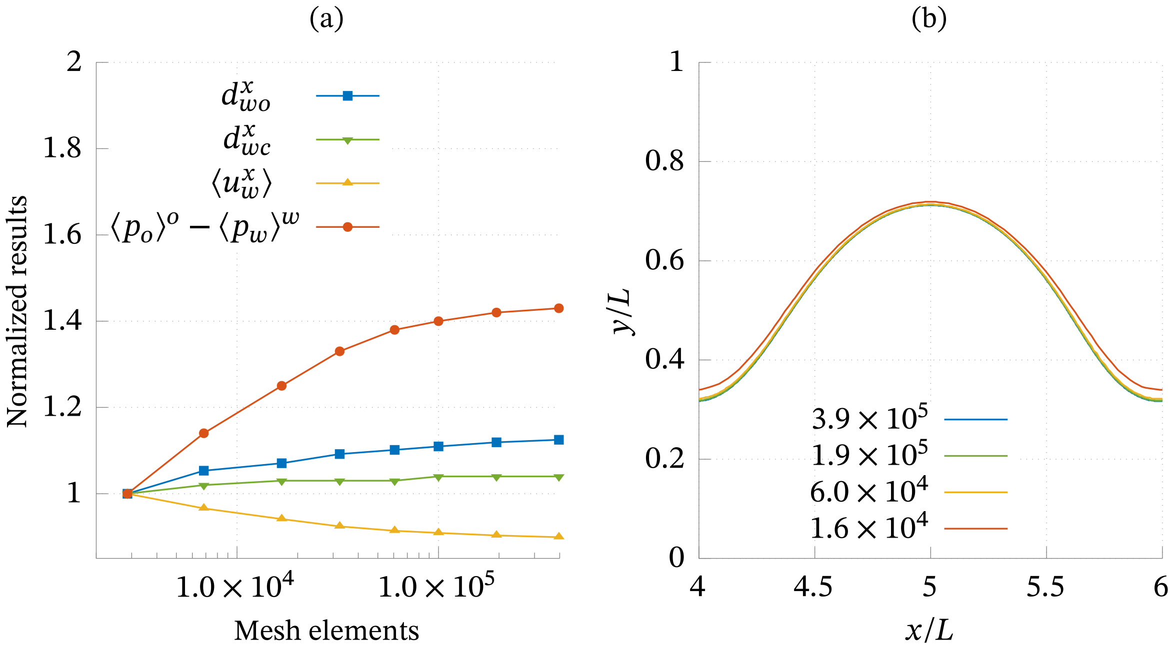

Figure 5: Mesh convergence study of (a) drag force (x-component) exerted upon the fluid-fluid boundary (blue line), drag force (x-component) exerted upon the cylindrical wedge interface (green), intrinsic average velocity of fluid w (yellow) and difference of the intrinsic average pressure (orange), all these results are normalized with respect to the result obtained with the coarser mesh and are computed at steady-state in UC3 (b) fluid-fluid interface position in UC3 at steady-state for different number of mesh elements in the whole geometry.

try. The dimensionless numbers for this study were $Ca = 1$, $f_f = 0.25$ and $M_w = 0.5$. We used a quadratic discretization for the velocity and the level-set function, and a linear discretization for the pressure. In Figure 5 (a) the results are normalized with respect to the coarser mesh result and the fluid-fluid interface postion is given in Figure 5 (b). These results were obtained in the third unit-cell (UC3) at steady-state and, except the difference in average intrinsic pressure, rapidly converge with the amount of mesh elements. In the following simulations, we used 1×10^5 meh elements in the whole domain.

4. Results and discussion

Before we turn to the study of drag force terms, we briefly discuss the flow regime observed along with the variation of the saturation with time.

Flow regime We observed that the two fluid phases remain continuous at all times and for the entire range of capillary and aspect ratio tested. At a point, the interface between the fluids becomes stationary and a stationary state is reached for every capillary and aspect ratio value. Initial, intermediate, and final configurations of the fluid repartition are presented in Figure 6. At steady-state, the fluid-fluid interface is periodic on the three central unit cells however the interface is slightly distort at the inlet and outlet cells, under the influence of boundary conditions.

The flow-regime observed is a film-flow regime in each case. This flow-regime is ideal to study the magnitude of fluids interaction terms, because the extent of the fluid-fluid interface is comparable to the extent of the fluid-solid interface and because the interface is parallel to the dominant direction of the flow and is therefore subject to high drag. In the following work, the results were obtained in the central unit cell UC3, and after steady-state was reached.

Saturation Wetting fluid saturation at steady-state decreases from 0.6 to 0.3 when the aperture between the plates decreases, as one can see in Figure 7, on which the saturation in UC3 is given as a function of the dimensionless aperture and different capillary numbers. As the aperture between the plates increases, the interface becomes flatter, while the film thickness at the throat pore level barely changes, so the saturation of the wetting fluid increases. This is noticeable on the embedded saturation fields in Figure 7. For an increasing capillary number the wetting fluid saturation slightly decreases, while with a more limited effect that aperture variation.

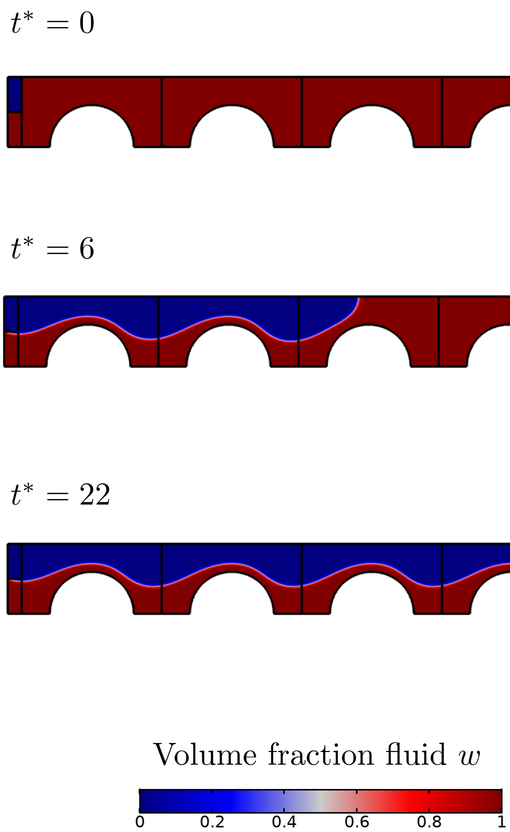

Figure 6: Fluids repartion along the superior half-row at the initial time, for an intermediate time and final time (steady-state reached) for $Ca = 0.05$, $f_f = 0.25$, $M_w = 0.5$ and $h^* = 0.25$. The dimensionless time is defined as $t^* = t \times (U_T/L)^{-1}$.

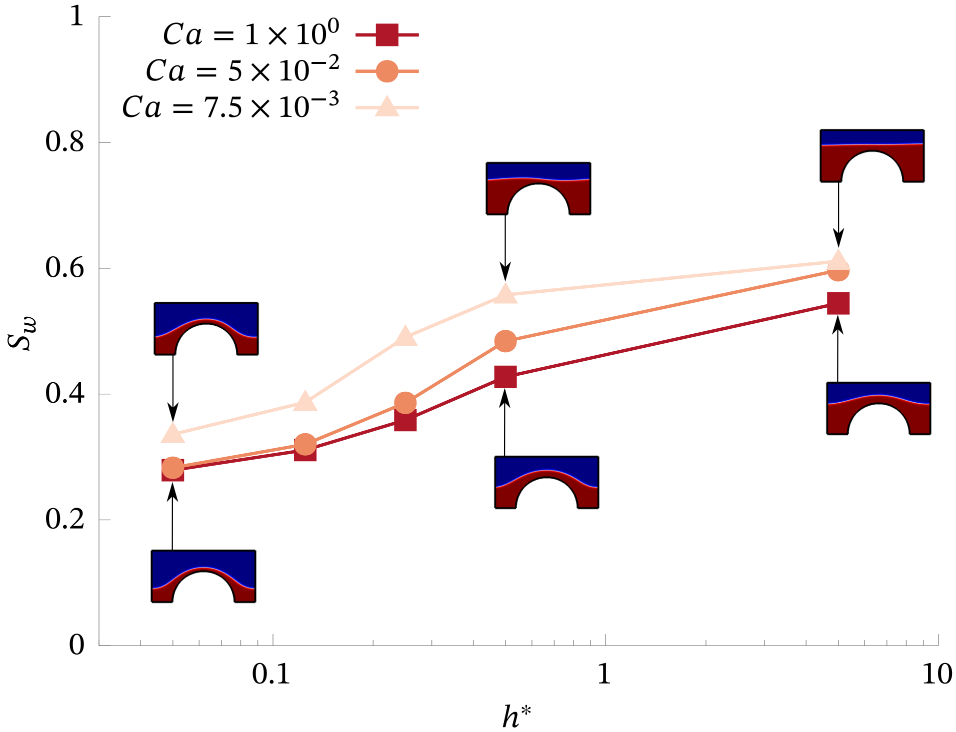

Figure 7: Wetting fluid saturation at steady-state in UC3 as a function of the dimensionless aperture and for different capillary numbers. Fields of the level-set function at steady-state in UC3 are given for selected value of the dimensionless aperture and $Ca = 1$ and $Ca = 7.5 \times 10^{-3}$.

Drag force Drag force exerted upon the fluid-fluid interface was computed according to Equation (13). The viscous part is obtained through the velocity gradient available at the $\phi = 0.5$ contour while the pressure part was obtained by application of the divergence theorem (see appendix section §B). The drag force exerted upon the wedge boundary, viscous and pressure part, was computed straight forward. In the following we are interested in the drag force compenent in the x-direction, i.e. the main flow direction. The total drag force (x-component) exerted upon the solid-fluid boundaries, denoted d_s^x, is the sum of the drag upon the wedge and upon the cell plates by both fluids. The total drag exerted upon the fluid-fluid interface, denoted d_f^x, is the sum of the contibution of each fluids, i.e. $d_f^x = d_{ow}^x + d_{wo}^x$. In the following, the x–component of the drag forces are expressed by unite surface area of unit-cell.

The total drag exerted upon the fluid-fluid interface reaches between 5 and 60% of the total drag exerted upon the solid-fluid boundaries, as can be seen in figure 8, on which we plot the ratio d_f^x/d_s^x as a function of the dimensionless aperture between the cell plates and for different capillary numbers. The main observation here is that the drag upon the fluid-fluid interface is not negligible here compared compared to the drag upon the solid-fluid interface. This could be anticipated by the flow regime, as discussed above, which is very favourable to the interactions between the two fluids. Interestingly, thepart of the drag upont the fluid-fluid interface increases, compared to the drag upon the solid-fluid interface, as the aperture between the plates decreases. At first glance, this may seem contradictory, since narrowing the aperture increases the pressure drop due to drag on the plates.

On Figure 9 we present the total drag upon either the solid-fluid interface or the fluid-fluid interface as a function of the dimensionless aperture. The drag forces at the fluid-fluid and solid-fluid interfaces logically increase as the capillary number increases. As the aperture between the plates decreases, the drag upon the fluid-solid interfaces also increases, which was to be expected. Regarding $Ca = 1$, both d_s^x and d_f^x evolve as h^{-2}. However, for smaller capillary numbers, the drag upon the fluid-fluid interface scales much as h^{-3} while the drag

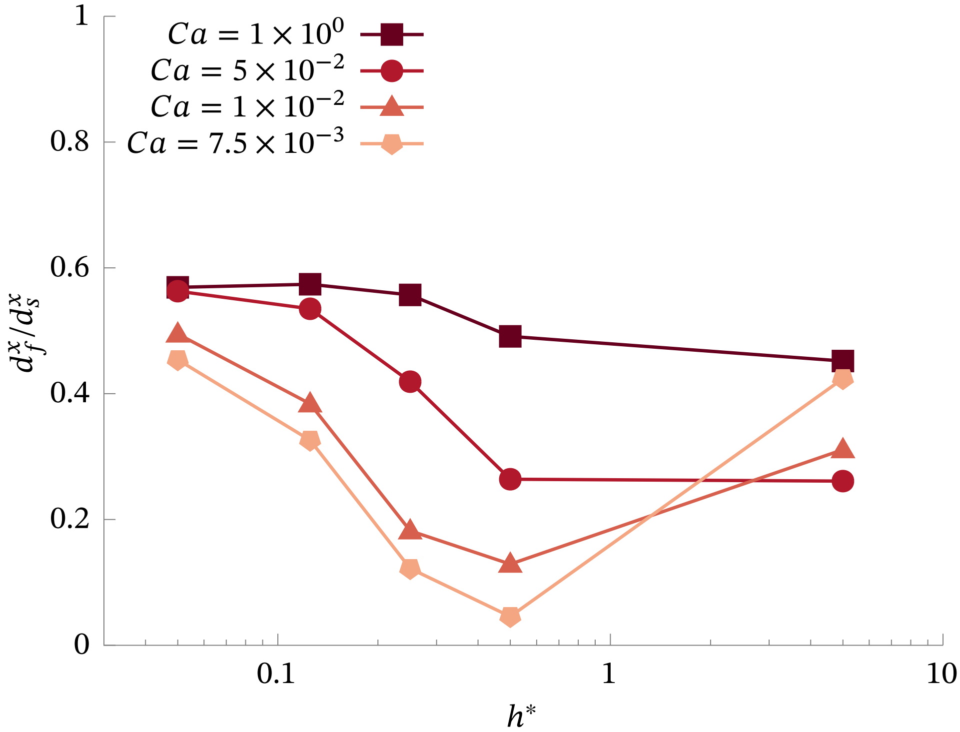

Figure 8: Ratio of the total drag force (x-component) exerted upon the fluid-fluid interface over the total drag force (x-component) exerted upon the fluid-solid interface as a function of the dimensionless aperture and for different capillary numbers. Results obtained at steady-state in UC3 for $f_f = 0.25$ and $M_w = 0.5$.

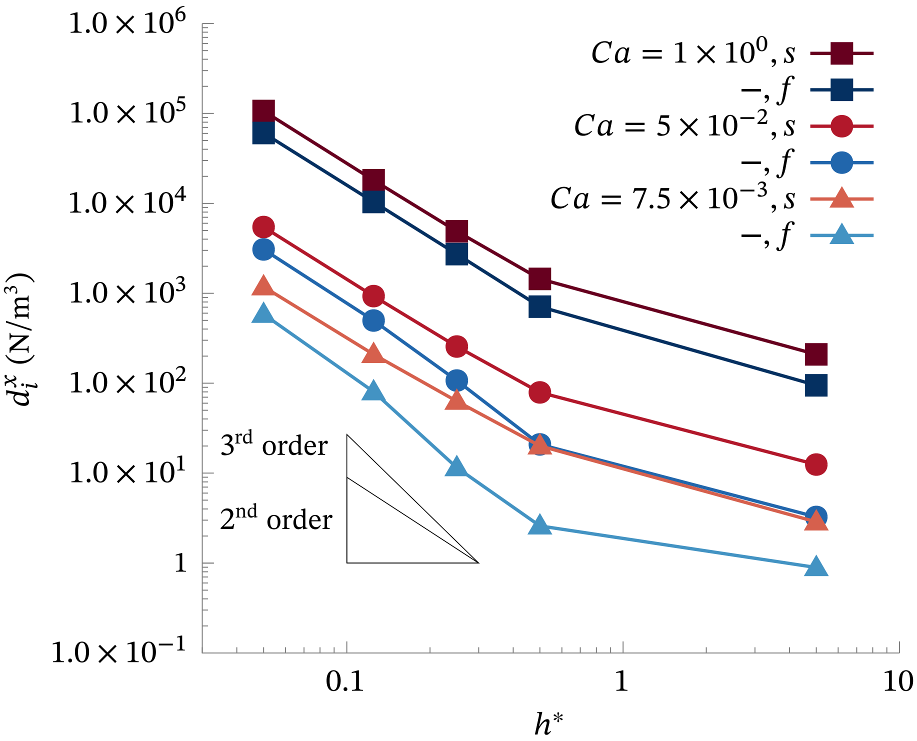

Figure 9: Total drag force exerted upon the solid-fluid boundaries and total drag force exerted upon the fluid-fluid interface as a function of the dimensionless aperture and for different values of the capillary number. Results obtained at steady-state in UC3 for $f_f = 0.25$ and $M_w = 0.5$.

upon the solid-fluid interface remains the same with a h^{-2} behaviour. This explains the influence of the capillary number and the origin of the variation in the ratio between the drag forces at the different interfaces. We mention that d_s^x is not entirely driven by the fluid friction upon the plates, as might be suggested by the h^{-2} behavior, in fact, the drag force upon the wedge is at least about 80% of the drag upon the plates, for $h^* = 1/20$.

On Figure 10 we present the viscous and the pressure part of the drag force exerted upon the fluid-fluid interface. For dimensionless aperture lower than $1/2$, the viscous part is negligible in front of the pressure part. Thus, the pressure drives the h^{-2} and h^{-3} behaviors, depending on the capillary number. As the plates aperture decreases, for a constant inlet velocity and a constant output pressure boundary condition; the pressure gradient through the micromodel increases, and the pressure force exerted by the flow on the solid-fluid and fluid-fluid interfaces as well. To better understand the effect of capillary number on pressure one can look at the pressure fields in UC3 for different capillary numbers and different apertures, as shown in Figure 11. Regarding $Ca = 1$, the pressure gradient along the x-direction across the cell is multiplied by 100 while the opening between the plates divided by ten, following Equation (7) . Now, for $Ca = 0.01$, and for the same change of plates aperture, the pressure gradient across the cell is multiplied by 2,000. A noteworthy feature ot the pressure gradient is how it compares with the pressure jump across the fluid-fluid interface because of its curavture. Indeed, for $Ca = 1$, the pressure jump and the pressure gradient are about the same order when $h^* = 0.5$, but the former becomes negligible in front of the latter as the opening decreases. This is to be expected since the pressure gradient increases as h^{-2}, whereas the pressure jump increases as h^{-1} since it is mainly induced by the curvature in the z-direction.

This last statement is veryfied in Figure 12 which shows the difference between the mean intrinsic pressures of the fluids as a function of the aperture between the plates along with the pressure jump produced by the curvature in the z-direction. There is a very slight discrepancy between the two quantities in the case of $Ca = 1$, but the difference between the average intrinsic pressures, regardless of the capillary number tested here, is caused by the curvature of the interface in the z-direction.

5. Conclusion

In this study we conducted direct simulations of depth-averaged two-phases flow, and we investigated the effect of the permeability on the drag forces exerted upon the different interfaces. The permeability was changed by varying the Darcean term which arising from the depth-averaging, thus without altering the in-plane geometry. These drag terms have to be modelled to obtain the macroscopic momentum transport equations but the drag ex-

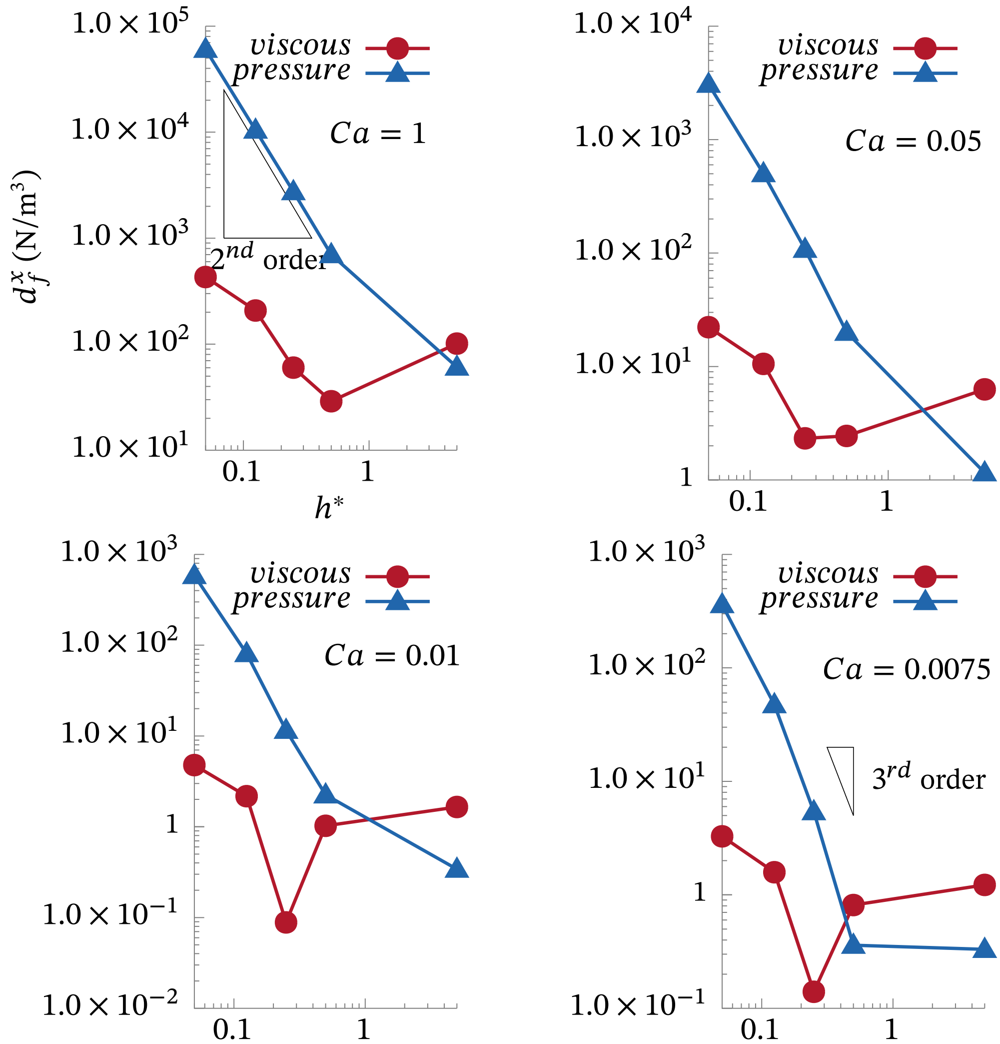

Figure 10: Pressure and viscous part of the total drag force exerted upon the fluid-fluid interface as a function of the dimensionless aperture and for different value of the capillary number. Results obtained at steady-state in UC3 for $f_f = 0.25$ and $M_w = 0.5$.

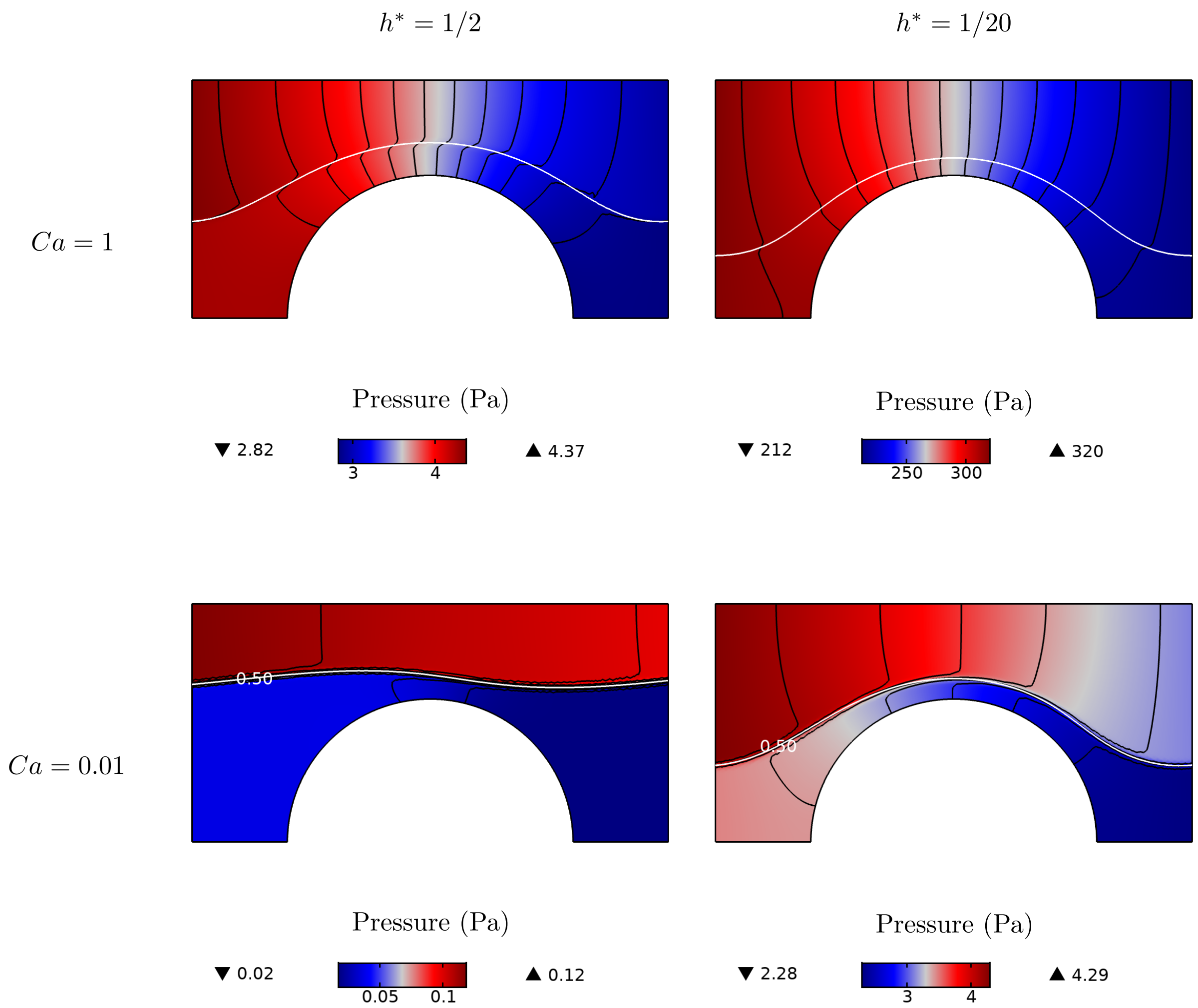

Figure 11: Pressure field in UC3 at steady-state for $Ca = 1$ and $Ca = 0.01$ and for different dimensionless aperture values $h^* = 0.5$ and $h^* = 0.05$. Isobar are representes in solid black lines and the fluid-fluid interface isdepicted with solid white lines.

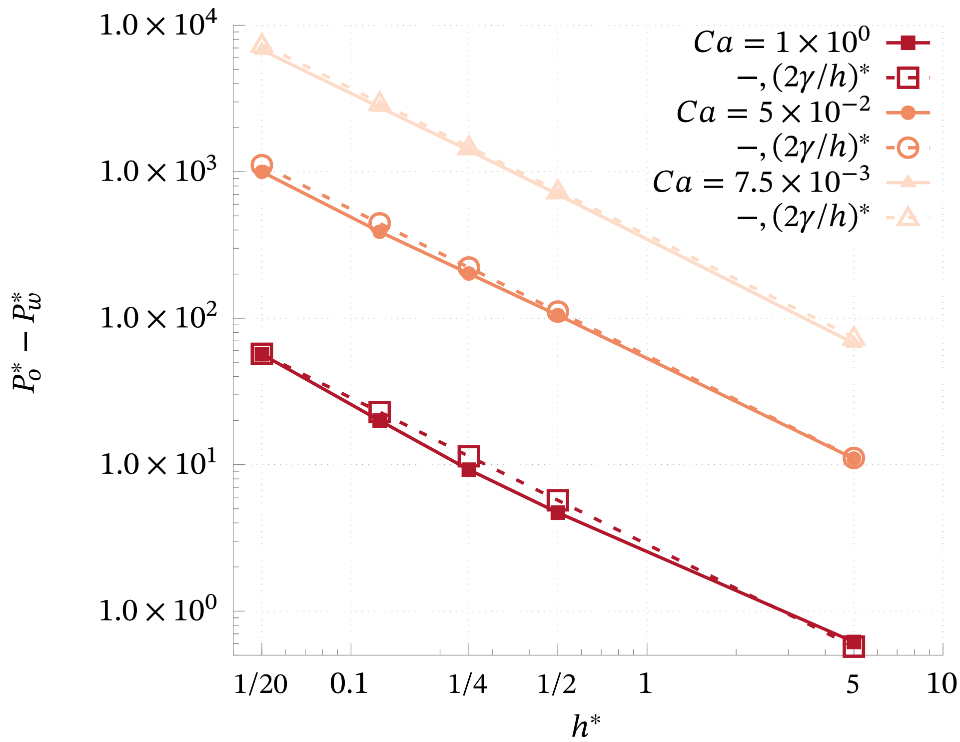

Figure 12: Dynamic pressure difference and pressure jump due to the interface curvature in the z-direction $(2\gamma/h)$ normalized with respect to the reference pressure $(U_T\mu_o/L)$ as a function of the dimensionless aperture and for different capillary numbers. Results obtained at steady-state in UC3 for $f_f = 0.25$ and $M_w = 0.5$.

erted upon the the fluid-fluid interface is commonly neglected for flow driven by capillarity forces. Here we focused on film-flow regime encountered in two-phases flows in high permeability porous media or in microfluidic devices. We found that the drag exerted upon the fluid-fluid interface should not be neglected into the momentum transport equations for film-flow regimes. Lower permeability does not make the drag force terms at the interface negligible as long as the flow regime remains a film regime. On the contrary, the drag force upon the fluid-fluid interface increases faster than the drag upon the fluid-solid interfaces, as the aperture between the plates decreases.

References

Attou, A., Boyer, C., Ferschneider, G., 1999. Modelling of the hydrodynamics of the cocurrent gas–liquid trickle flow through a trickle-bed reactor. Chemical Engineering Science 54, 785 – 802. doi:https://doi.org/10.1016/S0009-2509(98)00285-1.

Auriault, J., Sanchez-Palencia, E., 1986. Remarques sur la loi de darcy pour les écoulements biphasiques en milieu poreux. Journal of Theoretical and Applied Mechanics, Numéro Spécial , p141–156.

Avraam, D.G., Payatakes, A.C., 1995a. Flow regimes and relative permeabilities during steady-state two-phase flow in porous media. Journal of Fluid Mechanics 293, 207–236. doi:10.1017/S0022112095001698.

Avraam, D.G., Payatakes, A.C., 1995b. Generalized relative permeability coefficients during steady-state two-phase flow in porous media, and correlation with the flow mechanisms. Transport in Porous Media 20, 135–168. doi:10.1007/bf00616928.

Bacri, J.C., Chaouche, M., Salin, D., 1990. Modèle simple de perméabilités relatives croisées. Comptes rendus de l'Académie des sciences. Série 2, Mécanique, Physique, Chimie, Sciences de l'univers, Sciences de la Terre 311, 591–597.

Bentsen, R.G., Manai, A.A., 1993. On the use of conventional cocurrent and countercurrent effective permeabilities to estimate the four generalized permeability coefficients which arise in coupled, two-phase flow. Transport in Porous Media 11, 243–262.

Blunt, M.J., 2017. Multiphase flow in permeable media: A pore-scale perspective. Cambridge University Press.

Boyer, C., Volpi, C., Ferschneider, G., 2007. Hydrodynamics of trickle bed reactors at high pressure: Two-phase flow model for pressure drop and liquid holdup, formulation and experimental validation. Chemical Engineering Science 62, 7026–7032.

Carbonell, R., 2000. Multiphase flow models in packed beds. Oil & Gas Science and Technology 55, 417–425.

Clavier, R., Chikhi, N., Fichot, F., Quintard, M., 2017. Modeling of inertial multi-phase flows through high permeability porous media: Friction closure laws. International Journal of Multiphase Flow 91, 243–261.

Davit, Y., Quintard, M., 2018. One-phase and two-phase flow in highly permeable porous media. Heat Transfer Engineering , 1–19.

Dullien, F.A.L., 2012. Porous media: fluid transport and pore structure. Academic press.

Dullien, F.A.L., Dong, M., 1996. Experimental determination of the flow transport coefficients in the coupled equations of two-phase flow in porous media. Transport in Porous Media 25, 97–120. doi:10.1007/bf00141264.

Fetter, C.W., Boving, T., Kreamer, D., 2017. Contaminant hydrogeology. Waveland Press.

Guyon, E., Petit, L., Hulin, J.P., 1991. Hydrodynamique physique. interéditions.

Heshmati, M., Piri, M., 2018. Interfacial boundary conditions and residual trapping: A pore-scale investigation of the effects of wetting phase flow rate and viscosity using micro-particle image velocimetry. Fuel 224, 560 – 578. URL: http://www.sciencedirect.com/science/article/pii/S0016236118303971, doi:https://doi.org/10.1016/j.fuel.2018.03.010.

Horgue, P., Augier, F., Duru, P., Prat, M., Quintard, M., 2013. Experimental and numerical study of two-phase flows in arrays of cylinders. Chemical Engineering Science 102, 335–345.

Langaas, K., Papatzacos, P., 2001. Numerical investigations of the steady state relative permeability of a simplified porous medium. Transport in Porous Media 45, 241–266.

Lasseux, D., Quintard, M., Whitaker, S., 1996. Determination of permeability tensors for two-phase flow in homogeneous porous media: theory. Transport in Porous Media 24, 107–137.

Leverett, M., et al., 1941. Capillary behavior in porous solids. Transactions of the AIME 142, 152–169.

Li, H., Pan, C., Miller, C.T., 2005. Pore-scale investigation of viscous coupling effects for two-phase flow in porous media. Physical Review E 72. doi:10.1103/physreve.72.026705.

Marle, C.M., 1982. On macroscopic equations governing multiphase flow with diffusion and chemical reactions in porous media. International Journal of Engineering Science 20, 643 – 662. doi:https://doi.org/10.1016/0020-7225(82)90118-5.

Muskat, M., 1938. The flow of homogeneous fluids through porous media. Soil Science 46, 169.

Nagel, M., Gallaire, F., 2015. Boundary elements method for microfluidic two-phase flows in shallow channels. Computers & Fluids 107, 272–284.

Olsson, E., Kreiss, G., Zahedi, S., 2007. A conservative level set method for two phase flow ii. Journal of Computational Physics 225, 785 – 807. doi:https://doi.org/10.1016/j.jcp.2006.12.027.

Park, C.W., Homsy, G., 1984. Two-phase displacement in hele shaw cells: theory. Journal of Fluid Mechanics 139, 291–308.

Roman, S., Soulaine, C., Kovscek., A.R., 2019. Pore-scale visualization and characterization of viscous dissipation in porous media. Journal of Colloid and Interface Science doi:https://doi.org/10.1016/j.jcis.2019.09.072.

Rose, W., 1988. Measuring transport coefficients necessary for the description of coupled two-phase flow of immiscible fluids in porous media. Transport in Porous Media 3, 163–171. URL: https://doi.org/10.1007/BF00820343, doi:10.1007/BF00820343.

Rothman, D.H., 1990. Macroscopic laws for immiscible two-phase flow in porous media: Results from numerical experiments. Journal of Geophysical Research 95, 8663. doi:10.1029/jb095ib06p08663.

Saffman, P.G., Taylor, G.I., 1958. The penetration of a fluid into a porous medium or hele-shaw cell containing a more viscous liquid. Proceedings of the Royal Society of London. Series A. Mathematical and Physical Sciences 245, 312–329.

Salim, A., Fourar, M., Pironon, J., Sausse, J., 2008. Oil–water two-phase flow in microchannels: Flow patterns and pressure drop measurements. The Canadian Journal of Chemical Engineering 86, 978–988.

de Santos, J.M., Melli, T.R., Scriven, L.E., 1991. Mechanics of gas-liquid flow in packed-bed contactors. Annual Review of Fluid Mechanics 23, 233–260. doi:10.1146/annurev.fl.23.010191.001313.

Shams, M., Raeini, A.Q., Blunt, M.J., Bijeljic, B., 2018. A study to investigate viscous coupling effects on the hydraulic conductance of fluid layers in two-phase flow at the pore level. Journal of colloid and interface science 522, 299–310.

Sáez, A.E., Carbonell, R.G., 1985. hydrodynamic parameters for gas-liquid cocurrent flow in packed beds. AIChE Journal 31, 52–62. doi:10.1002/aic.690310105.

Tung, V., Dhir, V., 1988. A hydrodynamic model for two-phase flow through porous media. International journal of multiphase flow 14, 47–65.

Whitaker, S., 1986. Flow in porous media II: The governing equations for immiscible, two-phase flow. Transport in porous media 1, 105–125.

Whitaker, S., 2013. The method of volume averaging. volume 13. Springer Science & Business Media.

Wyckoff, R.D., Botset, H.G., 1936. The flow of gas-liquid mixtures through unconsolidated sands. Physics 7, 325–345.

Yiotis, A.G., Psihogios, J., Kainourgiakis, M.E., Papaioannou, A., Stubos, A.K., 2007. A lattice boltzmann study of viscous coupling effects in immiscible two-phase flow in porous media. Colloids and Surfaces A: Physicochemical and Engineering Aspects 300, 35 – 49. doi:https://doi.org/10.1016/j.colsurfa.2006.12.045. proceedings of the Fourth International TRI/Princeton Workshop.

Zarcone, C., Lenormand, R., 1994. Détermination expérimentale du couplage visqueux dans les écoulements diphasiques en milieu poreux. Comptes rendus de l'Académie des sciences. Série II, Mécanique, physique, chimie, astronomie 318, 1429–1435.

A. Approximation made near the interfaces

Approximation made with respect to the fluid-fluid interface We performed three-dimensional one-phase flow simulations into a micro-channel to determine the approximation made on the drag calculation when considering that the fluid-fluid contour can be translated along the z-direction.

One side of the microchannel is a half-circle wall to mimic a fluid-fluid interface while the opposite side is a flat wall (see Figure 13). Due to the construction of this geometry by extruding a cylinder to create the curved side of the channel, a special treatment has to be done to correctly meshed this part and we chose to build very small chamfers, as depicted in Figure 13. We computed the drag force per unit surface area on each sidewall of the microchannel and plot in Figure 14 the drag force exerted upon the curved side normalized with respect to the flat wall. The drag per unit surface area exerted upon the curved wall is roughly 70% of the drag per unit surface area upon the flat wall. Giving the greater extent of surface area for the curved wall, the difference regarding the drag computation is negligible.

B. Calculation of the pressure part of the drag upon the fluid-fluid interface

The pressure part of the drag exerted upon the fluid-fluid boundary Γ_{ij} by fluid i reads

$$\int_{\Gamma_{ij}} (p_i \mathbf{I}) \cdot \mathbf{n}_{ij} \, \mathrm{d}\Gamma, \tag{21}$$

where $p_i = p_i(x, y)$, $\mathbf{I}$ stands for the 2×2 identity matrix and $\mathbf{n}_{ij}$ is the normal unit vector at the fluid-fluid interface pointing toward fluid j. Equation (21) is obtained after applying the divergence theorem and subtracting the boundaries participitaion in an unit-cell other than from the fluid-fluid boundary, i.e., for fluid w,

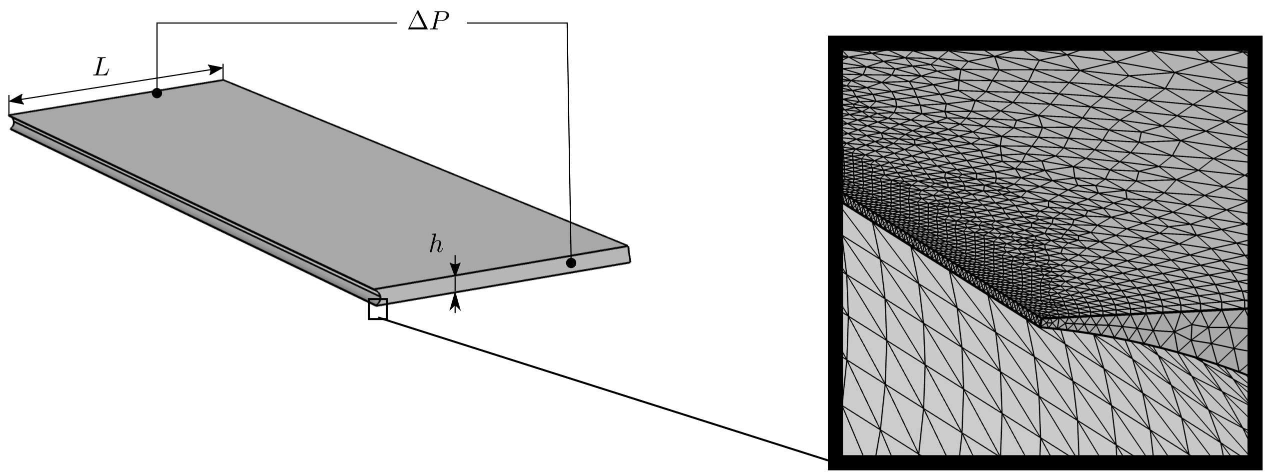

Figure 13: Microchannel with one side is a half-circle wall and the opposite side is a flat wall with $h/L = 1/16$ (left) and mesh detail at the sharp-edge left after the cylinder extrusion (right).

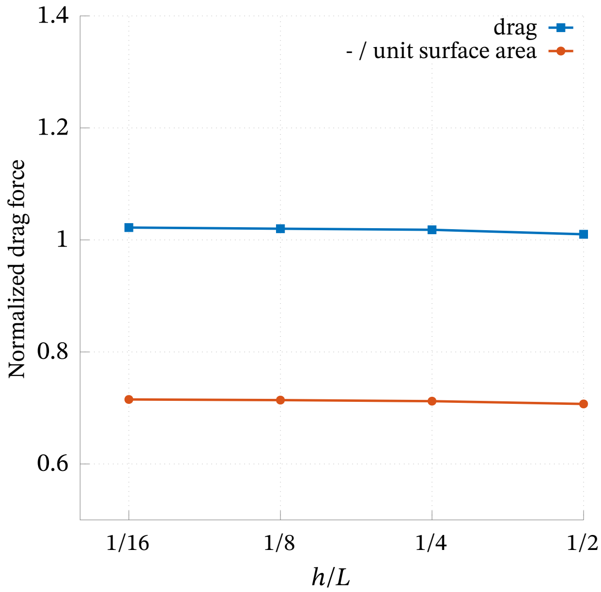

Figure 14: Drag force and drag force per unit surface area exerted upon the curved wall side of the microchannel normalized with respect to the drag force exerted upon the flat wall.

$$
\begin{aligned}
\int_{\Gamma_{wo}} \mathbf{n}_{wo} \cdot p_w \mathbf{I} \, \mathrm{d}\Gamma = \int_{S_w} \nabla \cdot (p_w \mathbf{I}) \, \mathrm{d}S + \int_{\Gamma_{w-left}} p_w \mathbf{I} \cdot \mathbf{n} \, \mathrm{d}\Gamma + \\
+ \int_{\Gamma_{w-top}} p_w \mathbf{I} \cdot \mathbf{n} \, \mathrm{d}\Gamma - \int_{\Gamma_{w-bot}} p_w \mathbf{I} \cdot \mathbf{n} \, \mathrm{d}\Gamma - \int_{\Gamma_{w-right}} p_w \mathbf{I} \cdot \mathbf{n} \, \mathrm{d}\Gamma - \int_{\Gamma_{w-cyl}} p_w \mathbf{I} \cdot \mathbf{n} \, \mathrm{d}\Gamma,
\end{aligned}
\tag{22}
$$

where the change of sign allows to take into account the change of orientation of the normal. Regarding the x-component, the integrals on the top and bottom boundaries vanish, and regarding fluid o, the integral on the cylinder's boundary vanishes, since only fluid w is in contact with the wedges.